Supporting Information for

Ultra-rapid Microwave-assisted Synthesis of Layered Ultrathin birnessite $K_{0.17}MnO_2$ Nanosheets for Efficient Energy Storage

Jinbao Zhu,[1] Qiuyang Li,[1] Wentuan Bi,[1] Liangfei Bai,[1] Xiaodong Zhang,[1] Jingfang Zhou,[2] and Yi Xie*[1]

[1]Division of Nanomaterials and Nanochemistry, Hefei National Laboratory for Physical Science at Microscale, University of Science and Technology of China, Hefei, Anhui, 230026, P. R. China;

To whom correspondence should be addressed. E-mail: yxie@ustc.edu.cn,

[2]Ian Wark Research Institute, University of South Australia, Mawson Lakes, SA, 5095,

Table of contents

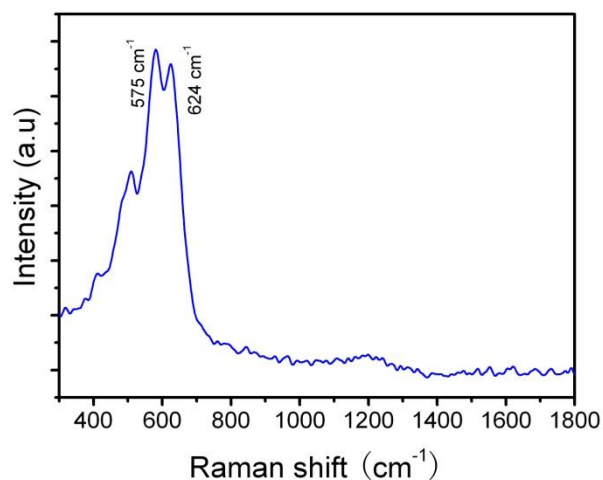## S1.　The Raman spectrum of as-obtained K-bir-LUNSs

Figure S1. The Raman spectrum of as-obtained K-bir-LUNSs, the perks across the 500-700 cm^{-1} region were attributed to the stretching mode of MnO_6 octahedra. The peak at 575 cm^{-1} is definitely deformation modes of Mn-O-Mn chain in the MnO_6 octahedral lattice, while the band at 624 cm^{-1} can be assigned to the symmetric stretching vibration of Mn-O in the MnO_6 group, [1] which is consistant with other birnessite nanostructure reported previously.[2] Thus, the Raman spectrum show a single sextet and thus provide clear evidence for the formation of high-quality birnessite $K_{0.17}MnO_2$.

S2. The survey XPS spectra of K-bir-LUNSs
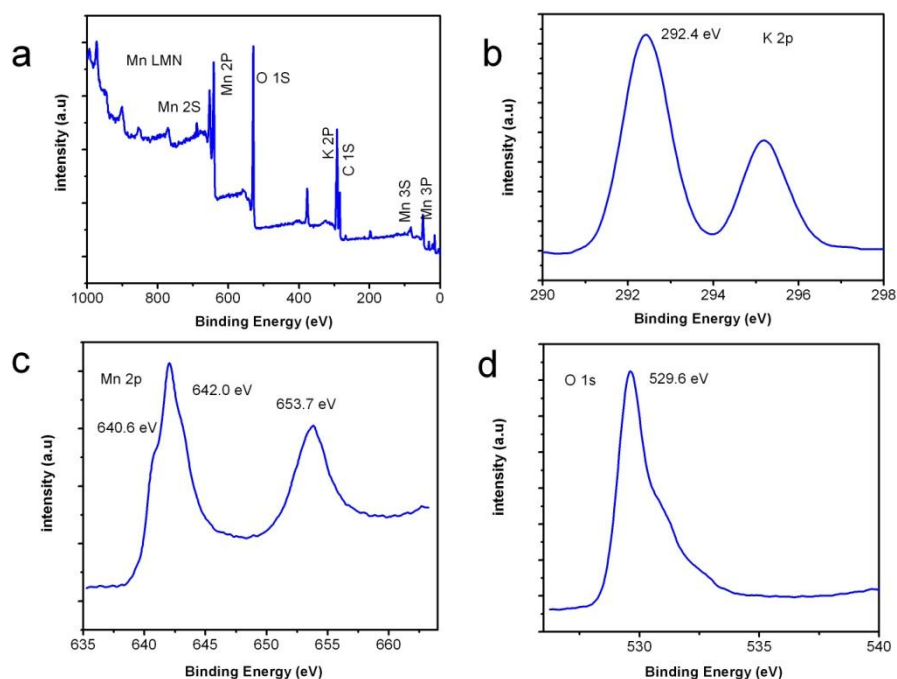
Figure S2. XPS spectra of K-bir-LUNSs showing (a) the survey spectrum; (b) K2p; (c) Mn2p; (d) O1s regions of birnessite $K_{0.17}MnO_2$.

The chemical composition and the valence state of as-prepared K-bir-LUNSs were investigated by X-ray photoelectron spectroscopy (XPS), confirming that product only consists of the elements K, Mn and O without any undesirable elements detected (Figure S2a). The initial K 2p peaks are symmetric, narrow, and devoid of satellite peaks, suggesting indicative of monovalent potassium (Figure S2b). The peaks of Mn $2p_{3/2}$ at 642.0 eV and $2p_{1/2}$ at 653.7 eV, with a spin-energy separation of 11.7 eV, demonstrate the existence of MnO_2 (Figure S2c).[3] It is necessary to note that the peak of O 1s includes a spiking at 529.6 eV and a relatively weak peak at 531.3 eV, which correspond to two kinds of oxygen: one in the lattice of $[MnO_6]$ octahedra, and the other in the interlayer H_2O (Figure S2d).[4] All these results indicate that the as-obtained product is high-quality birnessite $K_{0.17}MnO_2$, and the XPS spectra show no evident impurities detected in the sample (resolution limit:1 at.%).

S3. The UV-Vis spectra of as-prepared K-bir-LUNSs colloidal suspension
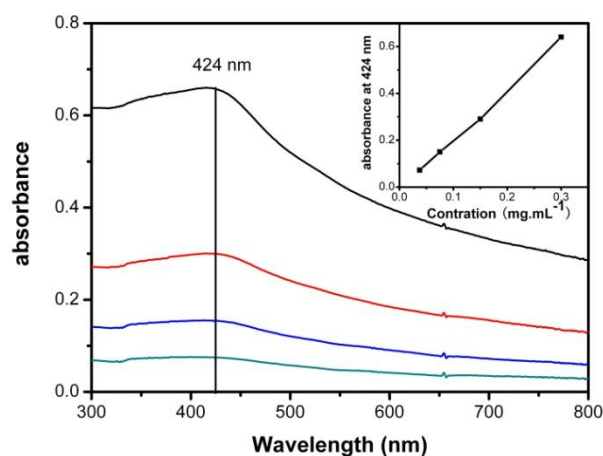
Figure S3. UV-Vis spectra and adsorbance (inset) at 424 nm for the colloidal suspensions at various K-bir-LUNSs concentrations.

The UV/Vis absorption spectrum of the colloidal suspension is shown in Figure S3. The absorbance at 424 nm is linearly proportional to the concentration range, which strongly suggests the absence of the agglomeration of prepared nanosheets (inset Figure S3). The blue-shifted UV-Vis peak could be ascribed to the quantum confinement effect with decreasing number of layers and hence indicates intrinsic ultrathin thickness (Figure S3). The molar extinction coefficient (ε) at the peak maxima (424 nm) was confirmed to be 2.05×10^2 $mol^{-1}dm^3cm^{-1}$, giving the direct and solid parameter to determinate the concentration of colloidal nanosheets.

S4.   The XRD pattern of as-obtained hausmannite Mn_3O_4
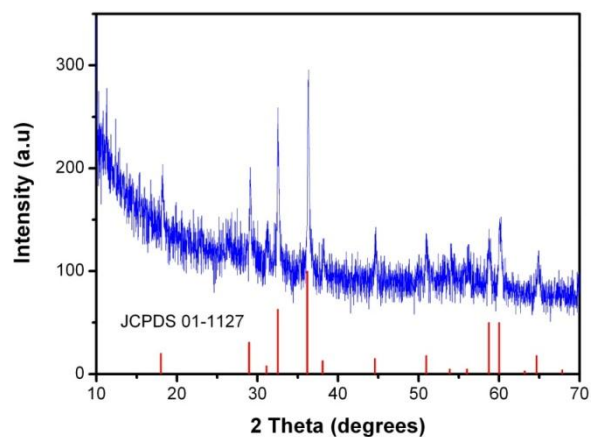
Figure S4. The XRD pattern of as-obtained hausmannite Mn_3O_4 prepared at 120 $^{\circ}$C for 24 h in the wet-chemical hydrothermal route, indicating the crucial role of the non-thermal effects of microwave dielectric heating for the formation the layer-type MnO_2 (the amorphous product was obtained within 3h in the hydrothermal route). The role of non-thermal effects, having their origin in the inherent characteristics of microwaves, is still rather speculative and ranges from lowering the Gibbs activation energy to increase of the collision efficiency by mutual orientation of polar molecules and possible excitement of rotational or vibrational transitions.[5]

S5. The TEM images of sample with glycerol as reducing agent and reactive medium
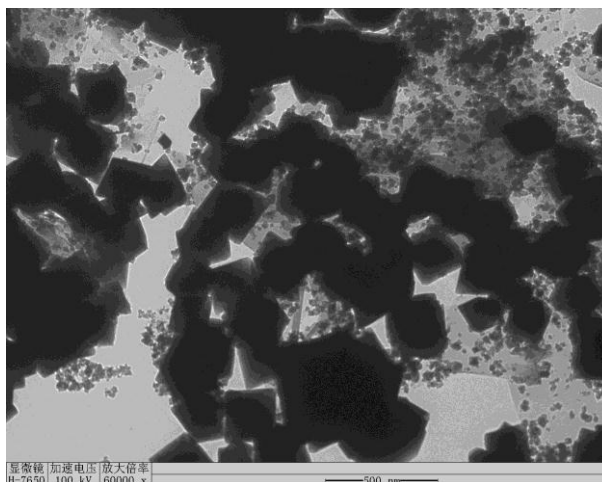
Figure S5. The TEM images of sample with glycerol as reducing agent and reaction medium.

In order to confirm the role of ethylene glycol in this route, other organic polyalcohol, such as glycerol, was used instead of ethylene glycol under other same synthetic procedure. Besides the ultrathin nanosheets in the product, large-quantity of nanocrystals with a size of ～200 nm were also clearly detected, indicating that ethylene glycol was confirmed to be a more suitable reducing reagent and reactive medium for the preparation of K-bir-LUNSs.

S6. The characteristics of ultrathin Na-type birnessite nanosheets
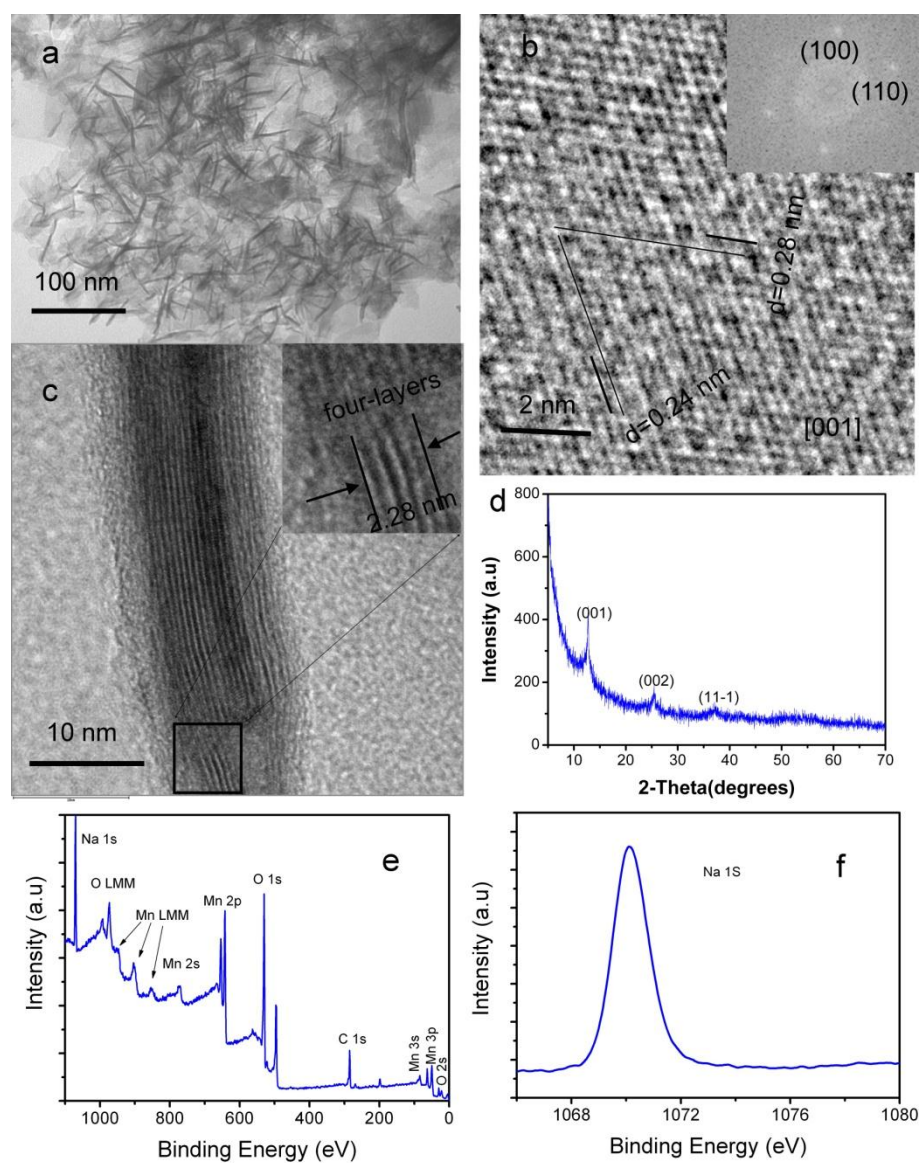
Figure S6. a) The TEM images of as-obtained ultrathin Na-type birnessite nanosheets; b) High-resolution TEM image and corresponding FFT pattern recorded near the edge of the nanosheets; c) the top view of High-resolution TEM image; d) The XRD pattern of ultrathin Na-type birnessite nanosheets-based film, displaying the highly preferred [001] orientation; e) Survey XPS spectrum of the as-obtained Na-type birnessite; f) High-resolution XPS spectrum of Na 1s. The binding energies found using XPS are corrected for specimen charging by referencing the C 1s line to 284.85 eV.

Compared with potassium ions, sodium ions with smaller ionic radius also favor the formation

of similar layered structures. Similar ultrathin Na-type brinessite nanosheets with a thickness of only 2.3 nm can also be obtained if by using NaOH instead during the same synthesis procedure (Figure S6), demonstrating the universality of this synthetic strategy in extensive to those layered structures. The TEM image clearly shows large-quantity of sheet-like morphology (Figure S6a). The obvious crystalline lattice of the nanosheets showed lattice spacings of approximately 0.24 and 0.28 nm, which can be characterized as the (100) and (110) planes of Na-type birnessite, respectively (Figure S6b). These results indicate that the well-crystallized nanosheets were spread perpendicularly to the c axis of birnessite. The hexagonal-shaped Fourier transform pattern is a typical feature of the reciprocal lattice projected along [001] zone axis, revealing that the as-obtained atomically-thick Na-type brinessite nanosheets grow along the ab plane of the monoclinic structure and that facets at the top and bottom surfaces are exposed. The interplanar spacing measured from the top view of HRTEM image is 0.57 nm on average (Figure S6c), which is smaller than the interlayer distance of 0.7 nm detected from the XRD pattern, attributing to the loss of the interlayer water in high vacuum of the microscope. In addition, the thickness of ∼2.3 nm was also directly determined from the top-view high-resolution TEM (HRTEM) image of the folded edge of an individual nanosheet (Figure S5c). Owing to the fact that it is currently infeasible to perform the X-ray diffraction pattern (XRD) characterization on an individual nanosheet, a layer-by-layer assembly strategy was adopted to fabricate ultrathin nanosheets based film. As shown in Fig. S6d, the XRD pattern of the ultrathin Na-type birnessite nanosheets-based film could be readily indexed to be monoclinic Na-type birnessite (JCPDS No.43-1456) without any undesirable phases (such as Mn_3O_4, $MnOOH$, Mn_2O_3) and also displayed the highly preferred [001] orientation. This not only revealed the high orientation of the ultrathin Na-type birnessite nanosheets-based film, but also illustrated that the ultrathin Na-type birnessite nanosheets had a preferred [001] orientation, fairly consisting with the HRTEM and FFT results (Figure S6b). In order to further confirm the chemical composition and the valence state, the XPS survey spectrum reveals that the as-obtained sample only consists of the elements Na, Mn and O without any undesirable elements detected (Figure S6e). The binding energy obtained in our XPS analysis was corrected for specimen charging by referencing the C1s line to 284.85 eV. The high-resolution XPS for the Na 1s region (Figure S6f) shows the core level at 1070.1 eV with the dominant Na signal assigned to Na^+.[6] All these results indicate that the as-obtained product is monoclinic Na-type birnessite, and the XPS spectra show no evident impurities detected in the samples (resolution limit:1 at.%). Thus, these results clearly illustrated that (001)-oriented ultrathin Na-type birnessite nanosheets with a thickness of only 2.3 nm were successfully prepared by microwave-assisted route, demonstrating the universality of this synthetic strategy in extensive to other ultrathin alkali metals-type birnessite nanosheets.

S7. The XRD pattern of corresponding bulk counterpart
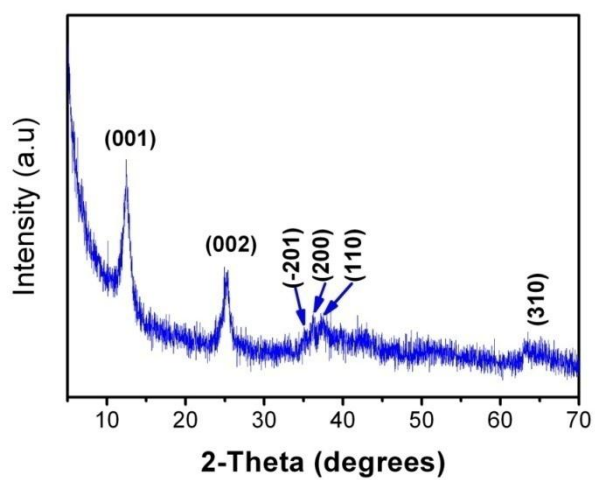
Figure S7. The XRD pattern of corresponding bulk counterpart.

## S8. The BET surface areas of as-obtained K-bir-LUNSs and bulk counterpart
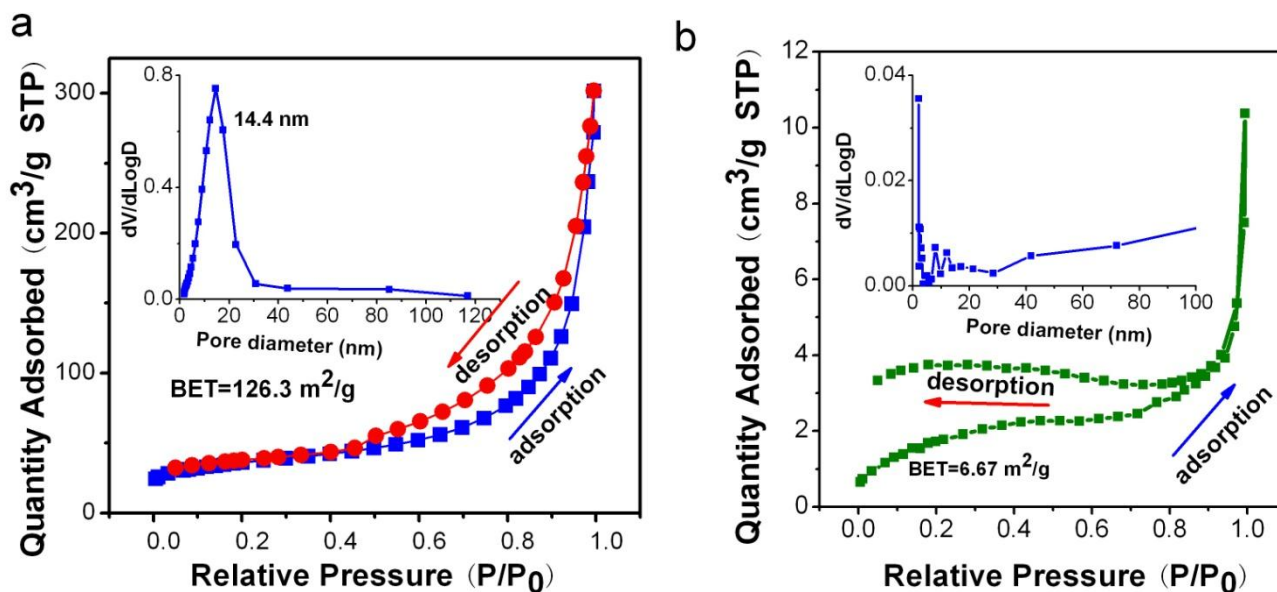
Figure S8. The N_2 adsorption-desorption isotherms and corresponding pore size distribution of a) K-bir-LUNSs and b) bulk counterpart calculated by Barretl-Joyner-Halenda (BJH) method from desorption branch.

The specific surface areas and porous nature of the products were further investigated by nitrogen adsorption/desorption measurements conducted at 77 K. The isotherms of K-bir-LUNSs can be classified as type IV isotherms, revealing that the material is composed of aggregates (loose assemblages) of sheet-like particles forming slit-like pores.[7] The as-obtained K-bir-LUNSs have a huge BET surface areas of 126.3 m^2/g with an average pore diameter of 14.4 nm and a pore volume of 0.344 cm^3/g (Figure S8a), higher than previously reported values of MnO_2 nanostructures and inorganic graphene analogues.[8] However, the specific surface area of bulk counterpart is only 6.67 m^2/g with irregular pore diameter and a pore volume of 0.01 cm^3/g (Figure S8b). The low surface areas of nanoparticles should be attributed to the larger crystal size resulting from aggregation in pyrolysis.

Owing to their unique morphology of finite in-plane size and well-defined layered structure, it is expected that laterally confined ultrathin nanosheets can significantly enhanced the host capabilities of active electrode materials arising from highly enhanced surface areas and easier accessibilities of guest molecules.[9] In this case, the synergic advantages of K-bir-LUNSs including both high specific surface areas and large inter-spacing volume, permitting adequate electrode-electrolyte contact and facile ion diffusion, endow them with eminently enhanced electrochemical performance.

S9. The Cyclic voltammograms curves measured with different scan rates for K-bir-LUNSs pseudosupercapacitors
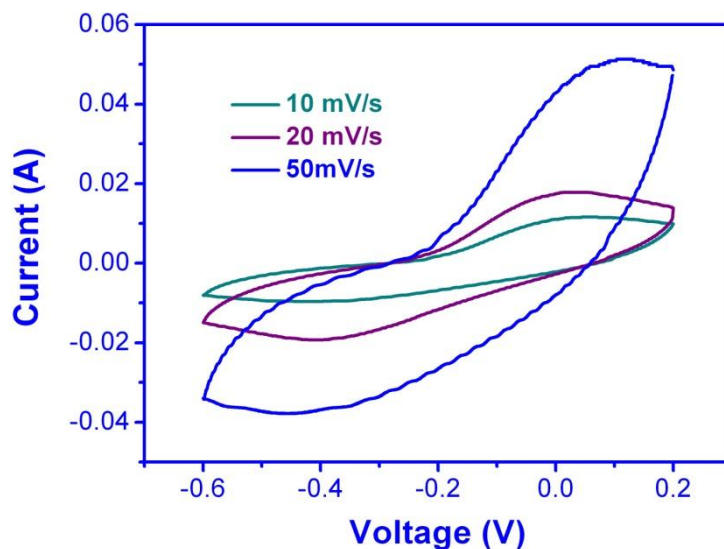
Figure S9. The Cyclic voltammograms curves measured with different scan rates for K-bir-LUNSs pseudocapacitors. The symmetrical oxidation peak and reduction peak indicated the existence of a highly reversible redox reaction, corresponding to K^+ insertion/extraction process *via* the reaction $K_xMnO_2 + (1-x)K^+ + (1-x)e^- \leftrightarrow MnOOK$ (Figure S7).[10]

S10. The galvanostatic charge-discharge curve of the K-bir-LUNSs measured at 5 A/g
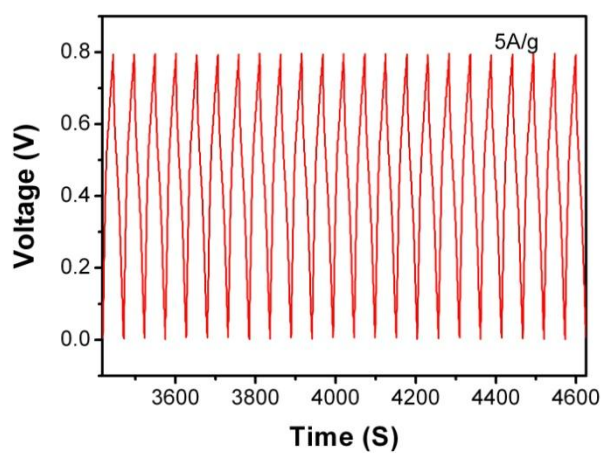
Figure S10. Galvanostatic charge-discharge curve of the K-bir-LUNSs measured at large current density of 5 A/g. The as-measured galvanostatic charge-discharge curve did not exhibit obvious changes, suggesting the excellent cycling stability of K-bir-LUNSs at fast charging.

S11. Nyquist plots of K-bir-LUNSs and bulk counterpart after cycled
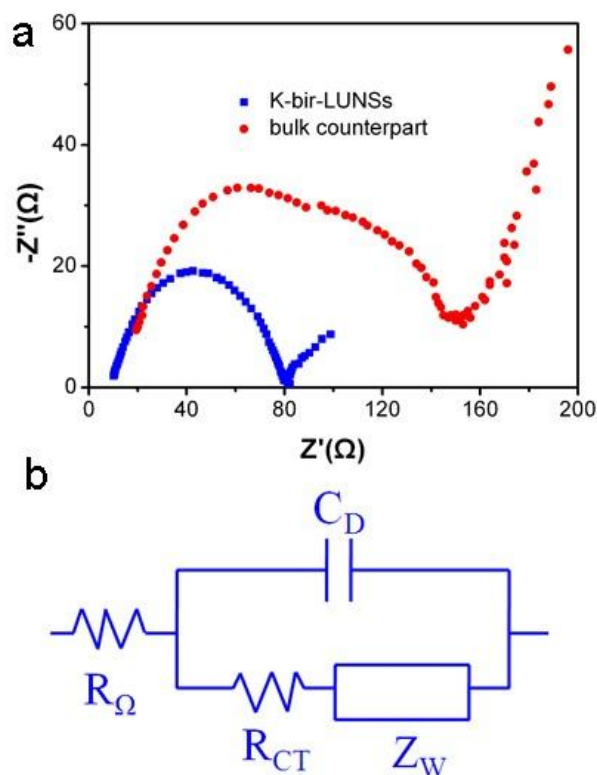
Figure S11. a) Nyquist plots of K-bir-LUNSs and bulk counterpart obtained by applying a sine wave with amplitude of 10.0 mV over the frequency range 100 kHz–0.1 Hz. b) Randles equivalent circuit for K-bir-LUNSs and bulk counterpart electrode/electrolyte interface. R_Ω is the ohmic resistance, CD is the double-layer capacitance, R_{CT} is the charge transfer resistance, and Z_W is the Warburg impedance describing the solid-state diffusion of Li^+ in active materials.[11]

In order to understand why K-bir-LUNSs exhibit such a superior electrochemical performance compared to bulk counterpart, AC impedance measurements were performed after cycled. The Nyquist plots show that the diameter of the semicircle for K-bir-LUNSs in the high–medium frequency region is much smaller than that of bulk counterpart, which suggests that atomically-thick nanosheets possess lower contact and charge-transfer resistances (Figure S11a).[12] The kinetic differences of K-bir-LUNSs and bulk counterpart electrodes were further investigated by modeling AC impendence spectra based on the modified Randles equivalent circuit (Figure S11b). The values of the ohmic resistance R_Ω and charge-transfer resistance R_{CT} were 13.09 and 60.84 Ω respectively,

in the case of K-bir-LUNSs, which were significantly lower than those of bulk counterpart (24.14 and109.9 Ω). This result confirmed that the ultrathin nanosheets not only could preserve the high conductivity of the overall electrode, but also largely improve the electrochemical activity during the cycle processes.

Table 1. Loss factor of different solvents

Table 1: Loss factor (tan δ) of different solvents[13]

Solvent	tan δ	Solvent	tan δ
ethylene glycol	1.350	DMF	0.161
ethanol	0.940	1,2-dichloroethane	0.127
DMSO	0.823	water	0.123
2-propanol	0.799	chlorobenzene	0.101
formic acid	0.722	chloroform	0.091
methanol	0.659	acetonitrile	0.062
nitrobenzene	0.589	ethyl acetate	0.059
1-butanol	0.571	acetone	0.054
2-butanol	0.447	tetrahydrofuran	0.047
1,2-dichlorobenzene	0.280	dichloromethane	0.042
NMP	0.275	toluene	0.040
acetic acid	0.174	hexane	0.020

Date from ref.[13]; 2.45 GHz, 20 ℃

Two parameters define the dielectric properties of a substance: (i) the dielectric constant ε', describing the ability to be polarized by the electric field, and (ii) the dielectric loss ε'', indicating the efficiency with which electromagnetic radiation is converted into heat. The ratio of these two parameters defines the dielectric loss tangent $\tan\delta = \varepsilon'/\varepsilon''$.[5] This loss factor provides a measure for the ability of a material to convert electromagnetic energy into heat at a given frequency and temperature. A reaction medium with a high loss factor, i.e., with a high $\tan\delta$ value, is required for efficient absorption and rapid heating. Organic solvents are generally categorized in three different groups according to their high, medium, and low absorbing properties. High microwave absorbing solvents typically have a $\tan\delta > 0.5$, whereas medium and low absorbing solvents have values of 0.1–0.5 and < 0.1, respectively. [13] Solvents with high loss factors (measured at room temperature and 2.45 GHz) include ethylene glycol (1.350), ethanol (0.941) or dimethyl sulfoxide (0.825), whereas solvents without a permanent dipole moment are basically microwave transparent. In this context it is striking to point out that the high absorbing solvents results to polarize the conducting electrons, leading to a local ''hot spot'' effect on the sheet surface, which promotes nanosheets growth.

References

1. Z. P. Li, J. Q. Wang, Z. F. Wang, H. Q. Ran, Y. Li, X. X. Han and S. R. Yang, *New J Chem*, 2012, **36**, 1490-1495.

2. S. H. Liang, F. T. G. Bulgan, R. L. Zong and Y. F. Zhu, *J Phys Chem C*, 2008, **112**, 5307-5315.

3. Z. Fan, J. Yan, T. Wei, L. Zhi, G. Ning, T. Li and F. Wei, *Adv Funct Mater*, 2011, **21**, 2366-2375.

4. M. Toupin, T. Brousse and D. Belanger, *Chem Mater*, 2004, **16**, 3184-3190.

5. I. Bilecka and M. Niederberger, *Nanoscale*, 2010, **2**, 1358-1374.

6. Y. Xue, X. D. Zhang, J. J. Zhang, J. Wu, Y. F. Sun, Y. C. Tian and Y. Xie, *J Mater Chem*, 2012, **22**, 2560-2565.

7. C. Wang, Y. Zhou, M. Y. Ge, X. B. Xu, Z. L. Zhang and J. Z. Jiang, *J Am Chem Soc*, 2010, **132**, 46-+.

8. J. W. Seo, Y. W. Jun, S. W. Park, H. Nah, T. Moon, B. Park, J. G. Kim, Y. J. Kim and J. Cheon, *Angew Chem Int Edit*, 2007, **46**, 8828-8831.

9. D. Rangappa, K. D. Murukanahally, T. Tomai, A. Unemoto and I. Honma, *Nano Lett*, 2012, **12**, 1146-1151.

10. G. Zhao, J. Li, L. Jiang, H. Dong, X. Wang and W. Hu, *Chemical Science*, 2012, **3**, 433.

11. Y. M. Lin, P. R. Abel, A. Heller and C. B. Mullins, *J Phys Chem Lett*, 2011, **2**, 2885-2891.

12. S. B. Yang, X. L. Feng and K. Mullen, *Adv Mater*, 2011, **23**, 3575-+.

13. C. O. Kappe, *Angew Chem Int Edit*, 2004, **43**, 6250-6284.